Mid-infrared spectroscopy of starbursts : from Spitzer-IRS to JWST-MIRI

Martínez-Galarza, J.F.

CHAPTER 6

The spectral properties of JWST-MIRI: calibration of the Flight Model[1]

MIRI is the mid-infrared instrument for JWST. The instrument has been fully assembled and tested in the United Kingdom by an international consortium, and now awaits integration with the rest of the JWST observatory. In this chapter we describe the functionality and the performance of the MIRI integral field spectrometer. Using the method described in 5, we obtain the wavelength calibration of the spectrometer for its full wavelength range. This is the only calibration of the instrument available before in-orbit measurements are performed. We measure the wavelength ranges of the sub-bands, estimate the resolving power of the instrument, and investigate the shape of the unresolved spectral lines. We are able to verify compliance with most of the instrument requirements. In particular, the spectral resolving power of MIRI is well above the values required to perform the planned science.

[1]Partially based on MIRI FM test reports by J.R. Martínez-Galarza, A. Glauser, E. Schmalzl, F. Lahuis, J. Morrison

6.1 Introduction

The Mid-Infrared Instrument (MIRI) onboard JWST is the next milestone in space-based mid-infrared astronomy. It will provide imaging, spectroscopy and coronagraphy at wavelengths of 5 μm to 28 μm. An international partnership between the Jet Propulsion Laboratory and a nationally funded consortium of European institutes, worked together to design, assemble, and test MIRI. Today, MIRI is the first instrument that has been fully tested and is ready to be sent to the United States for integration with the rest of the JWST observatory. MIRI will be a crucial instrument for all four of the primary science themes for JWST, namely: *(a):* the discovery of the "first light"; *(b):* the assembly of galaxies: history of star formation, growth of black holes, production of heavy elements; *(c):* the understanding of how stars and planetary systems form; and *(d):* the evolution of planetary systems and conditions for life.

During the summer 2011, the Flight Model (FM) of the MIRI instrument was thoroughly tested both in performance and functionality at the Rutherford Appleton Laboratory near Oxford, in the United Kingdom, building up on the previous experience with the Verification Model (see Chapter 5). The purpose was to verify all instrumental requirements set by the MIRI science goals using the flight software. A large portion of the test campaign was dedicated to observations with the integral field spectrometer, a crucial component of the instrument. We have obtained test MRS data of both point and extended sources and used them to perform a full calibration of the spectrometer, both spatially and spectrally, which allows for a reconstruction of the 3-dimensional information from astronomical sources. The calibration includes a measurement of the spectrometer field of view (FOV) on the sky, the measurement of the spectral ranges and resolving power for each channel, and the reconstruction of the resulting datacube. These measurements are all crucial for the verification of the instrument requirements and predictions on the science that will be possible with MIRI.

In Chapter 5 we have presented a method for the wavelength calibration of the MIRI spectrometer, and successfully applied it to VM data for one of the spectrometer subbands. In this chapter we use the method to provide a full spectral calibration of the instrument, for its entire wavelength range. This provides the only reference to the spectral properties of MIRI before any on-flight calibrations become available. We use the calibrated datacubes and our calibration method to measure important spectral properties such as wavelength coverage and spectral resolving power. We then compare the results with the instrumental requirements set by the MIRI science. In §6.2 we present a description of the observational setup, the observations performed and the reduction pipeline used. In §6.3 we present the analysis tools and methods that we have used to perform the wavelength calibration. We discuss our results in §6.4 and compare them with the instrumental requirements to verify their compliance. We finish this chapter with a summary of our main findings in §6.5.

6.2 Observations

6.2.1 The test campaign and the observational setup

The MIRI Flight Model Test Campaign was carried out in the summer of 2011. The instrument was inside a cryogenic chamber that kept it close to the operational temperature of 7 K. A revised version of the MIRI Telescope Simulator (MTS) was used to provide the incoming beam, both for extended and point sources. The improvements of the MTS with respect to the VM version included a sharper point source (using pinholes of either 25 μm or 100 μm in diameter) and a full illumination of the MIRI FOV with the extended source, including both the imager and MRS fields of view. MIRI is equipped with a Contamination Control Cover (CCC) that blocks any incoming light if necessary. For dark exposures, the CCC was kept closed.

On board calibration sources were employed to provide flat fields for both the MIRI imager and the MRS. The MTS was also equipped with solid state etalons and edge filters that provided the synthetic etalon lines and absolute wavelength references used for the

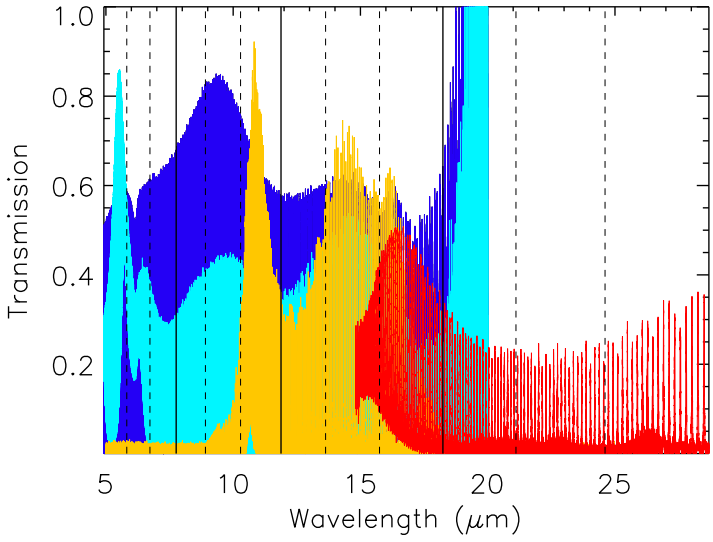

Figure 6.1 The transmission spectrum of the MTS solid state etalons, calibrated at high resolution prior to the test campaign. The color code is as follows. *Cyan:* Etalon 1A, *Blue:* Etalon 1B, *Yellow:* Etalon 2A, *Red:* Etalon 2B. The boundaries between channels are indicated by the solid lines, while sub-bands for each channel are separated by the dashed lines.

wavelength calibration of the spectrometer. A total of 337 hours of exposure time were employed for the performance tests of MIRI, of which about 65% were dedicated to the MRS. Most of the MRS exposure time was used for 100 μm pinhole observations, and a considerable part was used for extended source observations.

For all the observations the MTS blackbody (BB) source was at a temperature of 800 K, and the 100 μm pinhole was used to produce test point sources, with a fully open Variable Aperture System (VAS). Exposures were made with the slow readout mode for the MRS detectors.

6.2.2 Test data

To perform a full wavelength calibration of the four spectrometer channels, a large amount of observations were performed, including both extended and point sources. The extended source was used to fully illuminate the MRS FOV, and used the MTS solid state etalon filters (see Chapter 5) to generate a synthetic spectrum for the full MRS range. We also took etalon exposures with the 100 μm point source, to study variations of the resolving power with position of the source in the FOV.

Extended source observations

The wavelength calibration is achieved by measuring the positions of the unresolved spectral lines produced by the MTS etalon filters on the reconstructed cube. There are four of these etalon filters (1A, 1B, 2A, 2B), each optimized for one specific MRS channel. In Fig. 6.1 we show the coverage of each etalon within the MRS wavelength range, as measured prior to the test campaign.

We have measured the full MIRI spectrum for each of the solid state etalons whose transmission is shown in Fig. 6.1. For each etalon, three exposures were taken to cover the full 5 μm-29μm wavelength range, one exposure for each grating configuration: SHORT (A), MEDIUM (B) and LONG (C). Each exposure takes the corresponding sub-spectrum for all four channels simultaneously. The final spectrum for each etalon is thus composed of 12 sub-spectra. We have also obtained additional spectra of the long wavelength pass (LWP) and short wavelength pass (SWP) filters of the MTS Filter Wheel (FW), which provide absolute reference wavelengths for sub-bands 1C and 4B (with cutoff wavelengths at 6.6 μm and 21.5 μm respectively), as well as the spectrum of the unfiltered blackbody, which allows us to measure the instrumental response to the BB spectrum. Table 6.1 summarizes the combinations of etalons and grating positions for which we have obtained data.

To minimize the MTS FW movements, we first selected the desired etalon and then took three exposures corresponding to the three sub-spectra. Each of these exposures is followed by a background exposure. Only then we move on to the next etalon. After the etalon exposures are taken, we take the LWP, SWP and BB continuum exposures, with their respective backgrounds.

MTS Filter	Gratings A	Gratings B	Gratings C
1A	Yes	Yes	Yes
1B	Yes	Yes	Yes
2A	Yes	Yes	Yes
2B	Yes	Yes	Yes
LWP	No	No	Yes
SWP	No	Yes	No
BB Continuum	Yes	Yes	Yes

Table 6.1 Combinations of MTS filter positions and grating configurations for which we have obtained data.

Early exposures during the test campaign using etalon 1A and the dichroics set to LONG (hence, sub-band 1C), showed that our original approach for the exposure using 32 slow frames/integration and 4 integrations/exposure produced S/N ratios well beyond the necessary values, and hence for the rest of the campaign we reduced our exposures to 24 frames/integration, 4 integrations/exposure, which provided S/N above 50 for most of the MRS wavelength range. The instrument requirement associated to this measurement states that the wavelengths should be determined to an accuracy of at least 10% of the resolution element when the etalon lines are detected with a S/N of 50.

In order to investigate the temporal and mechanical wavelength stability, additional etalon exposures with the extended source were taken in different epochs of the test campaign, but given the limited test time, only etalons 1A and 2A were used. The different epochs were separated by at least one week. The first epoch is May 19, 2011, followed by epochs on June 21, and July 10. On July 21, an additional repeat of the etalon exposure was performed to check for stability after the grating mechanism had been configured.

Point source observations

For the point source etalon observations, we have performed a raster scan with the point source with five symmetric pointings with a step size of 1/4 of the slice width across the slice for two of the slices in each channel. These two slices are identified as Field 1 and Field 2 in each case. The origin of the 5-pointing raster pattern is at the nominal dither position. Fig. 6.2 shows the scan positions for all 4 channels.

The exposure times were adjusted to guarantee a peak to base S/N $\sim$ 100 for the reconstructed PSF. The resulting exposures were of 32 frames/integration, 2 integrations/exposure, in slow mode.

6.2.3 Data reduction

The data reduction consists on the following steps: *(i):* Creation of slope images from raw data registered on the two MRS detectors; *(ii):* Subtraction of the background and

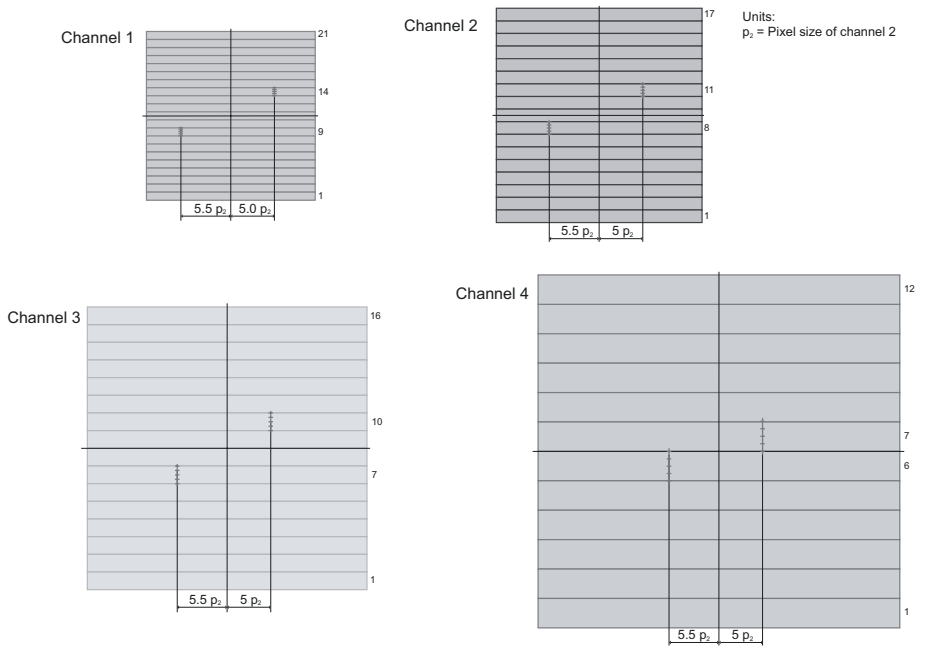

Figure 6.2 Field positions for the point source etalon exposures (small horizontal grey marks). Each channel is shown only once, but the pointings are repeated for all sub-bands.

flat-fielding of the resulting slope images, and *(iii):* Reconstruction of the datacube.

The following steps were performed on the raw data in preparation for the analysis. Version 5.0.7 of the *Data Handling and Analysis System* (DHAS) software [1] was used for all the datasets.

- The measured charge ramps on the detector are converted into slope values for each frame. The process involves correction of bad pixels, cosmic rays, as well as non-linearity corrections in the ramps. The average slope is calculated over multiple integrations. The resulting slope images are in counts per second (DN/s) and called level 2 data.
- Optionally, darks, pixel flats and fringe flats can be applied to the level 2 data. The fringe correction is customary in infrared detectors, because multiple reflections within the detector substrate create a Fabry-Perot fringing pattern.
- Spectral pixel flat fields are obtained from the spectrum of the BB extended source for all sub-bands. The flats are background subtracted and corrected by fringing.

[1] The DHAS software has been developed by Jane Morrison, University of Arizona.

We divide our slope images by these flats.

- No fringe flats were applied to the level 2 data, since not all fringe flats were available by the time of the analysis. Our tests show that at the S/N obtained, not including the fringe flats does not affect the measured centroids of the etalon lines by more than a few percent of the resolution element. The resulting data are level 3 files.

- Data cubes are built from the resulting MRS level 3 data. The dimensions of the resulting cubes are the along-slice spatial coordinate, α, the across-slice spatial coordinate, β (related to the slice number $N_{\rm slice}$ shown in Figs. 6.3 and 6.4), and the wavelength derived from the optical model, $\lambda_{\rm model}$. We discuss the details of the image reconstruction in §5.4.1.

- Background cubes are subtracted from the etalon, filter and continuum cubes, in a bin by bin basis. We perform the wavelength calibration on the resulting datacubes.

6.2.4 Reduced data

Extended source

In Figs. 6.3 and 6.4 we show slope images of the extended source MRS spectra for all four channels in sub-band 'A' (each figure shows one of the MRS detectors). We also show a zoomed view of the etalon lines for each channel in Fig. 6.5. These figures illustrate how the spectrum of an extended source looks like on the detector space, prior to the reconstruction of the datacube.

The etalon lines are detected with a signal-to-noise well above the required value of 50, over the full MRS wavelength range. An exception is sub-band 4C, which has a low throughput resulting from an inaccurate manufacturing of the grating. The low throughput for this sub-band reflects in a S/N of only a few for etalon lines on the long-wavelength end of the detector array. Nonetheless, etalon lines on the short-wavelength end of the detector (about a third of the pixels) are also detected with S/N over 50. For most of the other sub-bands the S/N is well above a value of 50 (about 900 in the middle of the spectral range). The high S/N in the etalon lines located on the regions of maximum transmission guarantees sufficient S/N in other regions of the etalon transmission range, in the overlapping regions with lines from different etalons (See Fig. 6.1). The resulting overlap pattern will be used later as an absolute reference wavelength for those sub-bands where no wave-pass filter was available.

Point source

For the point source etalon observations, the etalon lines were detected with a S/N varying from about 120 in Channel 1 to about 20 in Channel 4. The latter value is below the required S/N of 50, but for the long wavelength sub-bands where the S/N is lower, the

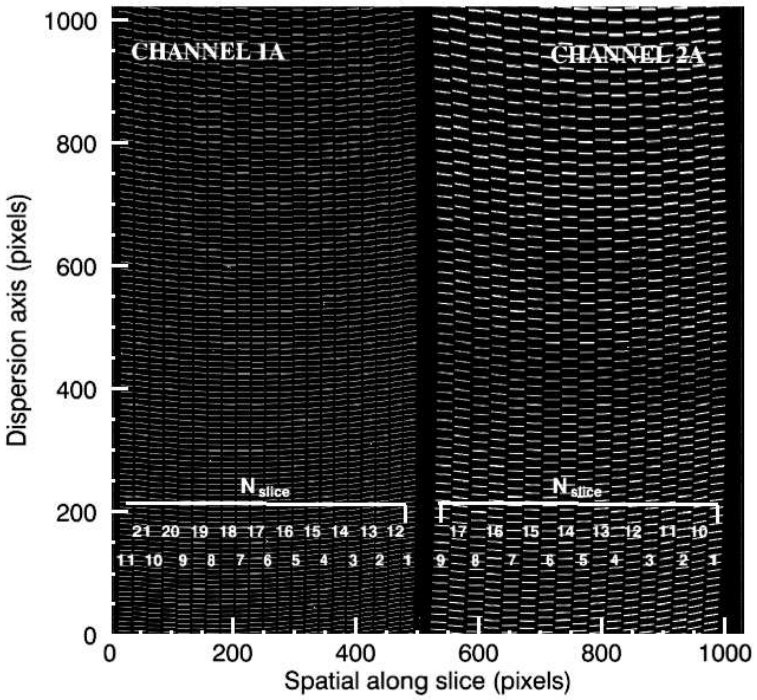

Figure 6.3 The slope image of the etalon 1A spectrum of an extended source, as registered on the SW detector for sub-bands 1A (left half of the detector) and 2A (right half of the detector).

etalon line profiles are better sampled on the detector, with FWMHs of about 3 pixels. In Fig. 6.6 we show and example of how the spectrum of a point source looks like on the detector array after the flat fielding has been applied. A comparison of this spectrum with the spectrum shown in Fig. 6.3 shows the reduced spatial extension of the point source as compared to the extended source. The etalon lines appear here as small dots, while in the case of the extended source they appear as horizontal lines. Adjacent slices on the detector do not correspond to neighbouring pixels in the FOV of the respective channel. This is the reason for the detection pattern observed on the detector.

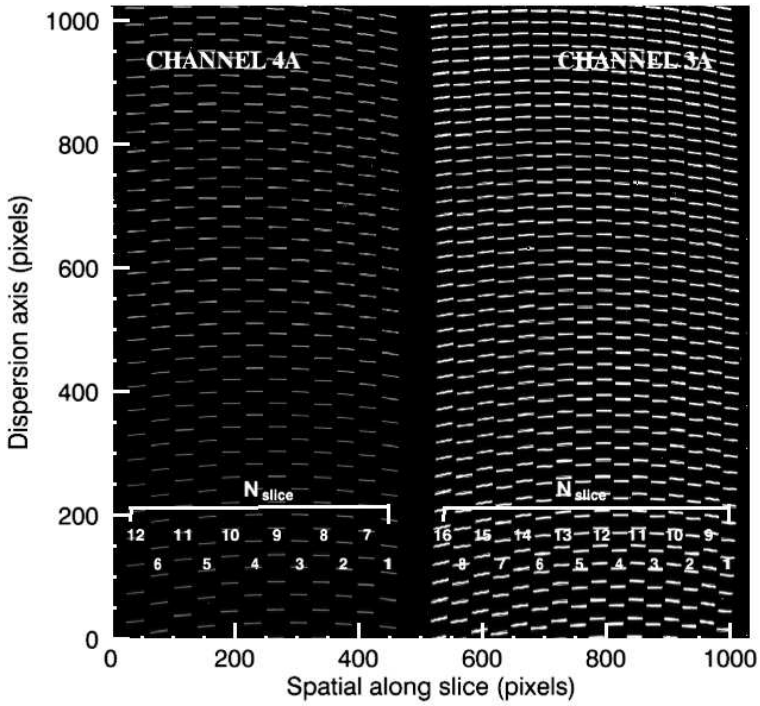

Figure 6.4 The slope image of the etalon 2A spectrum of an extended source, as registered on the LW detector for sub-bands 4A (left half of the detector) and 3A (right half of the detector).

6.3 Analysis

6.3.1 Wavelength characterisation

Up to this point, the resulting cubes have been constructed using the wavelengths resulting from the optical models, and hence these are the 'as-modelled' wavelengths. The purpose of the wavelength calibration is to update those wavelengths on the cube and detector space, to account for effects in detector and grating alignment, incidence angle of the light, and other effects in the as-built spectrometer that modify the predicted wavelengths. We now describe how this calibration was performed. The method builds on the experience obtained with VM data (see Chapter 5), but benefits from the much better data quality of the data obtained with the FM hardware.

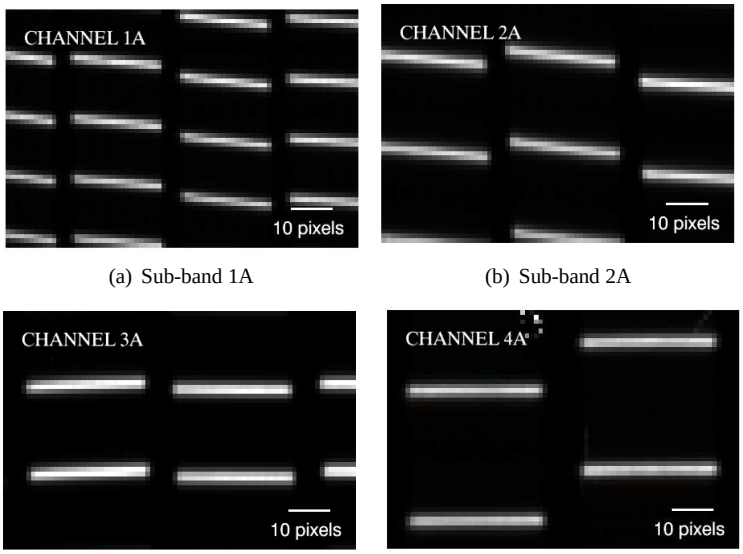

(a) Sub-band 1A (b) Sub-band 2A

(c) Sub-band 3A (d) Sub-band 4A

Figure 6.5 Detail of the unresolved etalon lines as registered on the detector, for the different MRS channels.

Extraction of the spectra

We extract the spectrum of each (α, β) pixel in the cube along the λ direction, for each of the 12 sub-bands. We end up with a spectrum for each spatial pixel in the FOV, and the image reconstruction algorithm relates each cube coordinate (α, β, λ) to a position (x, y) on the detector array. This is a one-to-one relation. The extraction is made using a single pixel aperture to avoid any potential smear of the line widths by combining different pixels. This is possible because we have an extended source that fully illuminates the FOV. A different approach is used for the extraction of a point source spectrum.

In Fig. 6.7 we show a single wavelength "slice" for each the four cubes resulting from an exposure with a particular grating configuration. The observed horizontal lines (particularly visible in sub-band 3A) that divide the FOV in two regions with different intensities are due to an uncorrected sky flat used in our analysis. The sky-flats are intended to correct for throughput variations in both the along-slice (α) and the across-slice (*beta*) directions, but they were not properly measured at the time of our analysis.

Gaussian fit to the etalon lines

In Fig. 6.8 we show a part of the extracted etalon spectrum for a particular (α, β) position. Shown are two different sub-bands 1A and 4A. We fit Gaussian profiles to the registered spectral lines to measure the position of their centroids and their widths. The Gaussian fit

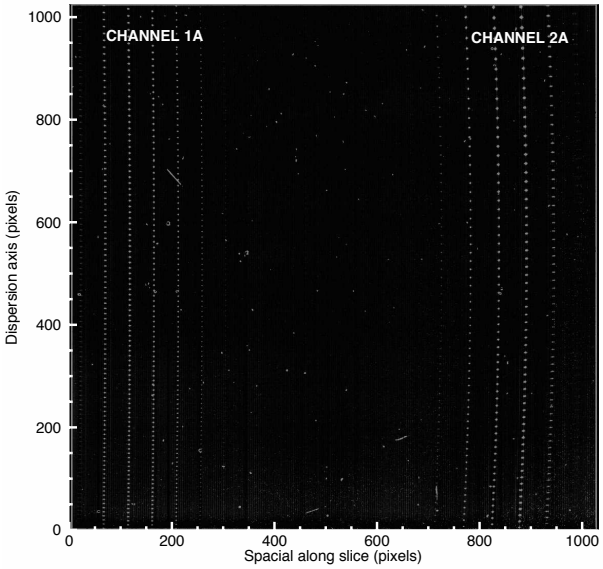

Figure 6.6 The slope image of the etalon 1A spectrum of a point source, as registered in the SW detector for sub-bands 1A (left half of the detector) and 2A (right half of the detector).

was performed in the bin space of the dispersion axis of the cube (λ), and not in wavelength space derived from the optical models, since those are precisely the wavelengths that we intend to derive and correct. By working on the bin space, we made no assumptions about the wavelengths. The fits provide a measure of the centroid of each line and their full width at half maxima (FWHM). Both quantities are measured in units of the cube bin.

The Gaussian fits provide an accurate measurement of the etalon line centroids in the cube space. Using the transformation described in §5.4.1 for the cube reconstruction, we can locate those centroids also in the detector space. With the signal to noise achieved, the accuracy in the line centroids is of the order of 2% of the resolution element for each sub-band. The wavelengths of the peaks are known to an accuracy of a few Angstroms from a previous high resolution measurement of the etalon transmission (see §6.3.2 for a discussion on the associated errors). These high resolution measurements were carried out using a IR spectrometer at the Rutherford Appleton Laboratory, at temperatures of $\sim 77\,K$ (cryogenic) and $\sim 77\,K$ (room), to study the centroid variations with temperature.

With the information of the line centroids and a set of relative reference wavelengths from the high resolution measurements, we only need an absolute wavelength reference in order to associate each centroid with its actual wavelength. This will be the base of a

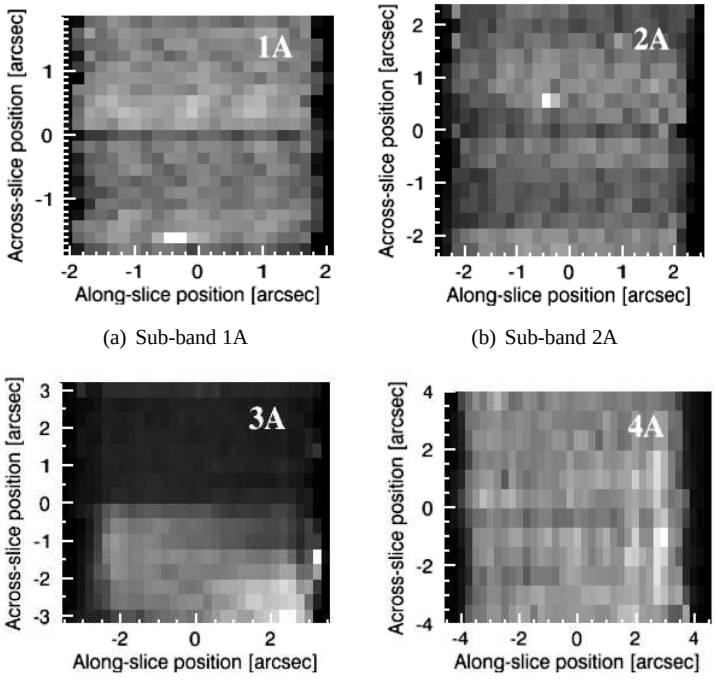

(a) Sub-band 1A (b) Sub-band 2A

(c) Sub-band 3A (d) Sub-band 4A

Figure 6.7 Single wavelength layers of the reconstructed images for the four MRS channels, with the gratings in 'A' configuration (short wavelengths). The pixel scale has been modified in each case to match the spatial dimensions.

dispersion relation between cube bins and wavelengths.

Absolute wavelength references

Building up on the experience from VM testing, we used the two wave-pass filters to obtain an absolute reference wavelength for those sub-bands where their cutoff wavelengths are registered. For FM testing, the much better quality of the detectors, as well as the possibility of longer integrations with the extended source resulted in a better measurement of the LWP filters response. Also, since the long-wavelength detector for channels 3 and 4 is now available, we can also measure the response of the SWP filter.

The transmission curve of both filters has been characterised prior to the test campaign at room temperature (295 K) and at a cryogenic temperature of 77 K. At this cryogenic temperature, the LWP filter has a cutoff wavelength near 6.6 μm (sub-band 1C), while the SWP has a cutoff wavelength near 21.5 μm (sub-band 4B). According to the telemetry data obtained during the test, the operating temperature of the LWP and SWP filters is

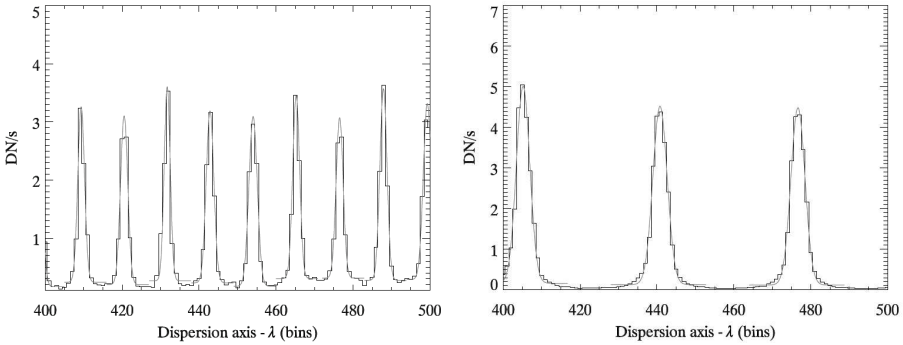

(a) Sub-band 1A (b) Sub-band 4A

Figure 6.8 Gaussian fits to the etalon lines for two of the sub-bands. The black lines is the MRS spectrum, and the lighter grey lines are the Gaussian fits.

about 34 K. A simple extrapolation from the transmission curves at room and cryogenic temperatures allowed us to conclude that the shift in the cutoff wavelength from a further decrease in temperature (to the operational 34 K) is less than the relative separation between etalon lines. This is important, since it meas that we rely on the much better accuracy of the centroid positions rather than the accuracy on the cutoff wavelength.

We obtained a measured transmission curve from the extracted spectra of the wave-pass filters and the blackbody continuum taken during the campaign. A comparison with the calibrated curves provided the absolute reference we were aiming for. The measured spectra of the LWP and SWP filters is the product of the actual filter response and the BB continuum, and hence we divide the measured spectra by the measured BB continuum. We correlate the resulting response curve with the reference transmission curve for each spatial position (α,β) in the FOVs of sub-bands 1C and 4B and in this way we obtain an absolute reference wavelength in the center of the cutoff slope. Fig. 6.9 shows the resulting correlations for a particular spatial coordinate.

For those sub-bands where no wave-pass filter is available as an absolute reference, we used a different approach to calibrate the wavelengths. The transmission of the etalon filters is optimized for but not limited to one MRS channel. That implies that for a given sub-band, etalon lines from more than one etalon filter are detected in different exposures. Therefore, for most of the sub-bands, we measure etalon lines from different etalons, that overlap with each other. The performance test was designed so that these overlapping etalon lines were detected with a S/N of at least 50. The resulting overlapping or beating pattern of the etalon lines for each sub-band is used as an absolute reference for wavelength. We use these overlaps for all remaining sub-bands.

For sub-band 4C the situation is more tricky. FM testing has revealed that the throughput for this sub-band is not optimal, and the etalon lines we detect in 4C have low S/N ratio, specially in the long wavelength end. Also, we have only detected lines from etalon 2B in this sub-band, and hence no overlap pattern was observed. We then looked for spec-

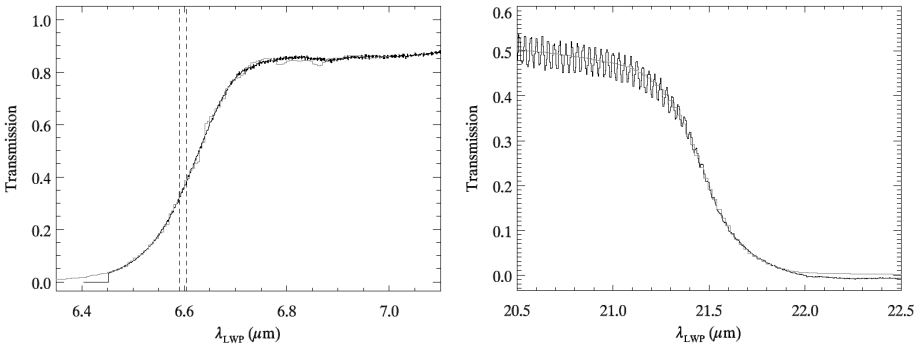

(a) LWP (b) SWP

Figure 6.9 The measured transmission curves of the LWP *(a)* and SWP *(b)* filters (black lines) correlated with the reference curves (lighter grey lines). The effect of fringing is more pronounced in sub-band 4B, where the SWP cutoff falls. The dashed lines indicate the separation between two adjacent etalon lines.

tral features that could serve as wavelength references. There is a broad absorption feature near the long wavelength end of this sub-band. While this feature remains unidentified, the fringe analysis showed that the feature is internal to MIRI. If we use the wavelengths predicted by the Zemax model, this feature can be associated to a wavelength of 27.8 μm as shown in Fig. 6.10. We use this feature as our "absolute" reference, but we are aware that it is model-dependent. While this might lead to an incorrect absolute calibration, it allows for a relative calibration of this sub-band.

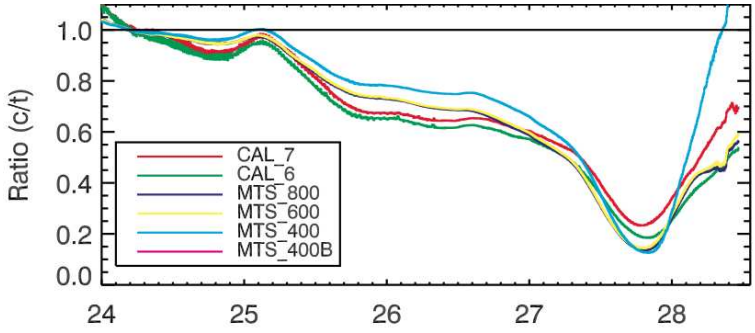

Figure 6.10 The broad absorption feature seen in sub-band 4C at approximately 28.7 microns, for the calibration source and the continuum of the MTS blackbody at different temperatures. The x axis is the Zemax wavelength (in μm). We use this feature as a wavelength reference for sub-band 4C.

Dispersion relation and unresolved line widths

We have fitted a second order polynomial to the resulting array of cube bins vs. wavelength for each (α,β) position in the field of view for each of the sub-bands. Deviation of the data with respect to polynomials of higher orders would be smaller than the required precision for this measurement. In Fig. 6.11 we show the dispersion relation as derived in this way for a particular FOV position in 2 of the sub-bands. Along the *y* axis, instead of the absolute wavelength, we have plotted the difference between the derived wavelengths and the Zemax wavelengths, in units of the resolution element for each sub-band. The dispersion slightly deviates from linear relations.

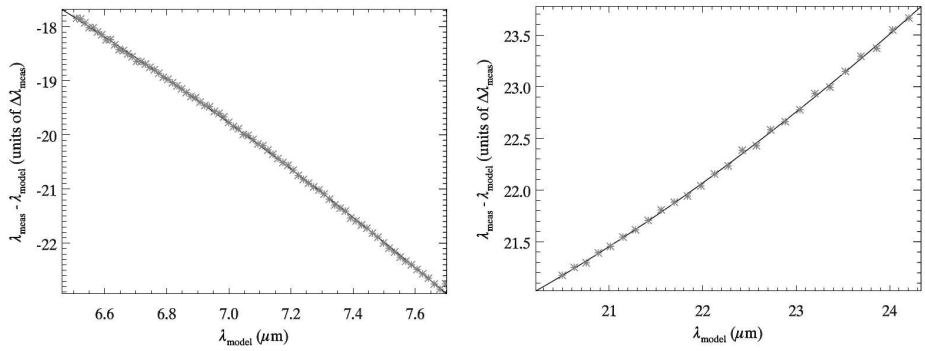

(a) Sub-band 1C (b) Sub-band 4B

Figure 6.11 The difference between the modelled and measured spectrograph dispersion, as a function of the Zemax wavelengths. The asterisks mark the measured centroids of the etalon lines, and the solid black line is the polynomial fit.

We used the same approach as in VM testing to estimate the resolving power. The FWHM of the unresolved etalon lines is a good estimate of the size of the resolution element at the particular wavelengths of the line centroids. From the Gaussian σ parameter (the Gaussian width) in our fits, we obtained the FWHM in units of cube bins using:

$$\text{FWHM} = \Delta\lambda = 2\ \sqrt{2\ln 2}\sigma \tag{6.1}$$

Using the derivative of the polynomial dispersion relation that we have fitted, we converted the FWHM to microns, and then we calculated $R = \lambda/\Delta\lambda$ for the full MRS range and for the totality of the field of view.

The conversion from the measured FWHMs in units of cube bins into equivalent FWHMs in detector pixels is not straightforward, because the cube spectral bin size is constant in wavelength and the size of the binning corresponds approximately to the detector pixel size at the shortest wavelength of each sub-channel. That means that, for a particular sub-band, a wavelength bin projected onto the detector has approximately the same size as a detector pixel only at the short wavelength end. At the long wavelength

end, its size is smaller than the detector pixel by approximately 20%. The reason for this change has to do with the binning method used for the cube reconstruction.

To assess the impact of this effect, we adopted two different approaches to calculate the FWHMs of the unresolved lines in pixels. In the first approach, we assumed a linear conversion between cube bins and detector pixels, simply by multiplying the measured FWHMs in cube bins by $N_{\rm bin}/N_{\rm pix}$, the ratio between total cube bins for the respective cube and the total number of detector pixels in the array in the wavelength dimension. This will slightly overestimate the size of the pixels in the long-wavelength end of each sub-band. In the second approach, we assumed a uniform decrease in the size of the pixel relative to the bin as we move towards longer wavelengths, in such a way that at the wavelength of the first (shortest wavelength) etalon line, the pixel is 95% the size of the bin, while at the position of the last (longest wavelength) etalon line, the pixel is 85% the size of the bin.

6.3.2 Uncertainties

Absolute and relative centroids of the etalon peaks

There are several sources of uncertainty involved in the determination of the dispersion relation as described in the previous section. Here we evaluate their impact on our results.

The first source of error comes from the uncertainty in the reference etalon peak positions, measured at high resolution before the testing. The positions of the peaks were measured at a resolution of $R \sim 10^5$ before testing at RAL at two different temperatures: room temperature ($\sim$ 295 K) and at a cryogenic temperature ($\sim$ 77 K). However, as revealed by the telemetry data acquired during testing, the operational temperature of the etalon filters in close to 34 K during the whole campaign. The etalon thickness and hence the positions of the etalon lines changes with temperature, due to the thermal properties of the material of which the etalons are made (ZnSe for etalons 1A, 1B and 2A and CdTe for etalon 2B). In order to estimate the shift in position of the line centroids from the measured 77 K to the 34 K operational temperature, we have extrapolated the etalon thickness at 34 K by using available literature data on the thermal expansion coefficient ($\alpha_{\rm thermal}$) of the mentioned materials (Browder & Ballard 1969, 1972, Smith & White 1975). In order to perform the extrapolation, we used the thicknesses at 295 K and 77 K, as derived from the etalon equation that gives the separation between peaks:

$$\Delta\lambda = \frac{\lambda_0^2}{2nl\cos(\eta)} \tag{6.2}$$

where n is the refractive index of vacuum ($n = 1$), l is the etalon thickness and η is the incidence angle of the light on the etalon filter (we assume $\eta = 0$). Fig. 6.12(a) shows the literature data used for the thermal expansion coefficient of ZnS, and Fig 6.12(b) shows the resulting extrapolation of the etalon thickness. We conclude that the shift in wavelengths of the peaks from 77 K to 34 K is negligible for the purposes of our analysis: a fraction of 2-4% of the resolution element for all sub-bands.

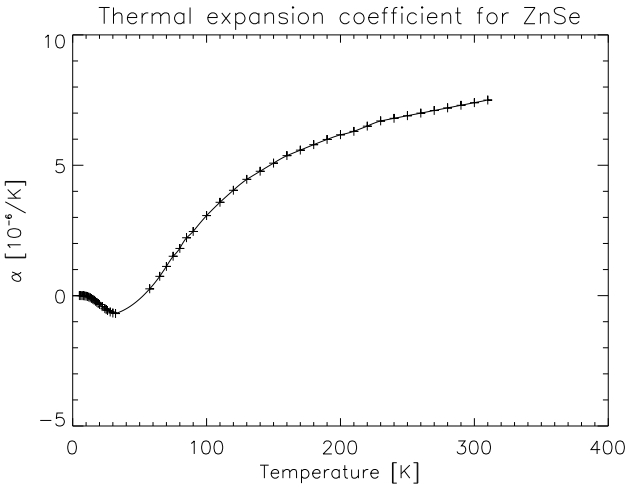

(a) Thermal expansion coefficient

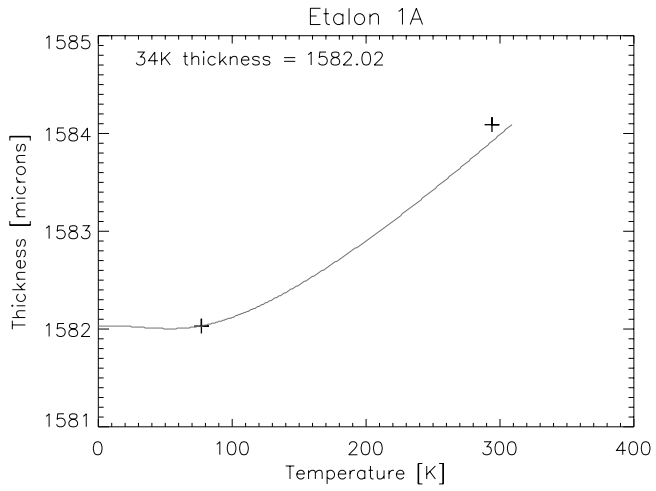

(b) Etalon thickness

Figure 6.12 *(a)* The thermal expansion coefficient ($\alpha_{\rm thermal}$) for ZnSe, from the literature (Browder & Ballard 1969, 1972, Smith & White 1975). *(b)* The extrapolated value of the etalon thickness for $T < 77$ K.

The combined effect of this wavelength shift with the uncertainty introduced by fitting the etalon lines with Gaussian profiles is still < 1% of the resolution element. Although

we have not done a similar analysis for the position of the cutoff wavelengths of the LWP and SWP filters, we do not expect a major change in their position at 34 K. Nevertheless, the accuracy needed for the cutoff wavelengths is set by the separation between neighbouring etalon lines, which is much larger than any shift due to temperature effects.

Another source of error for the wavelength calibration comes from the deviations of the measured line centroids with respect to the derived second-order polynomial dispersion relation. We have measured the standard deviation of the shift between the measured line positions and the value of the derived dispersion relation across the wavelength range, for all FOV positions in each sub-band. We then construct an histogram with the values of the measured absolute shifts, in units of microns. Fig. 6.13 shows the resulting histograms for two of the sub-bands.

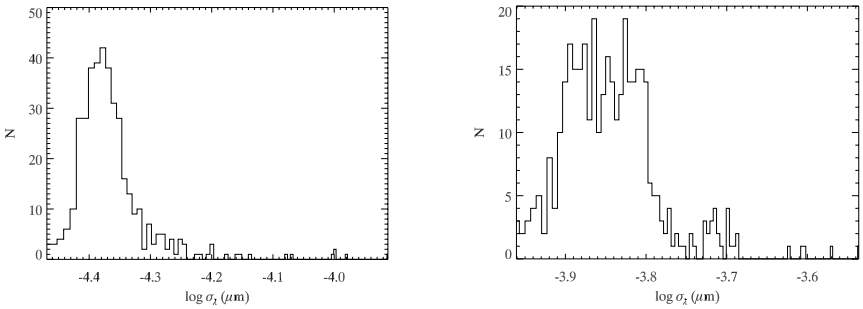

(a) Sub-band 1B (b) Sub-band 3B

Figure 6.13 Observed standard deviations from a second-order dispersion relation across the FOV for sub-bands 1B *(a)* and 3B *(b)*.

The figures imply that, on average, the deviation between the centroid positions and the derived dispersion relation is of the order of 1 Å, or about 2% of the resolution element for all sub-bands. This is the dominant error in our analysis, and it is at least one order of magnitude larger than the errors derived from Gaussian fitting of the lines and temperature variations. We thus consider that we know the wavelengths of the derived data cubes with uncertainties of 0.02 times the spectral resolution element.

An additional source of error is the fringing pattern associated with multiple reflections within the detector. As we have stated, we did not correct for fringing for the dataset in study. Although we were not able to quantify it for all channels, a comparison between the measured line positions before and after fringe correction for channel 1 revealed that applying such correction does not change the line centroids by more than our 2% of the resolution element, and hence our uncertainties are still dominated by the polynomial fit.

Resolving power

The observed etalon line profiles are the convolution of the intrinsic line shape and the spectral response of the MRS. The resolving power calculated here using only the FWHM

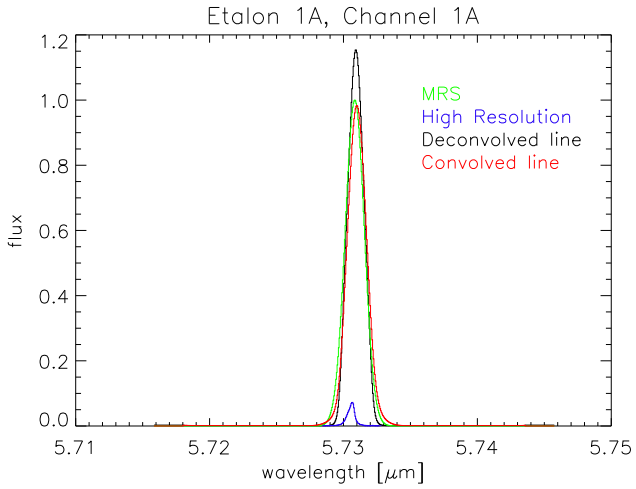

(a) Sub-band 1A

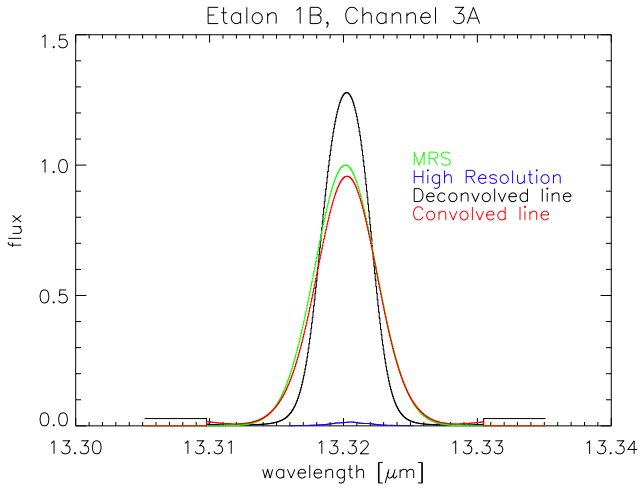

(b) Sub-band 3A

Figure 6.14 Deconvolution of the observed etalon lines (green) with the intrinsic line profile obtained from the high resolution observations (blue), for sub-bands 1A *(a)* and 3A *(b)*. The result is the instrument spectral response (black), which we have convolved again with the intrinsic profile to check the deconvolution. The recovered profile is shown in red.

of the unresolved etalon lines is thus jeopardized by the effect of the intrinsic line profiles. In order to estimate the errors introduced by this effect on the calculation of the resolv-

ing power, *R*, we have deconvolved the observed line shapes with the intrinsic shape of the lines, that we obtain from the high resolution measurements of the etalon transmission performed at RAL prior to testing. For this purpose, we used the IDL procedure `max_entropy`, which deconvolves the two profiles using the maximum entropy method. Fig. 6.14 shows the result of the deconvolution for two of the MRS channels.

The profile of the instrument spectral response, as obtained from the deconvolution, is narrower than the observed unresolved profile. This implies that the resolution calculated from the FWHM is an underestimate. We studied the effect of the deconvolution on the line widths across the full wavelength range of the MRS, using the method described. We conclude that the enhancement in resolving power resulting from the correction for the intrinsic line shape is between 10% and 20%. For a given sub-band, there is a smooth increase in this enhancement with wavelength. Also, the enhancement is larger in the long wavelength channels, where the intrinsic widths of the lines start to be comparable with the resolving power of the instrument.

6.4 Results and discussion

6.4.1 The resolving power of the MRS

In Table 6.2 we list the wavelength ranges and resolving powers that we have calculated for each of the MRS sub-bands using the methods described above. For each sub-band, we list a nominal value for the resolving power, *R*, corresponding to its measured value at the center of each band. We also list the size of the resolution element for each band, in detector pixels, using the two methods that we have described at the end of §6.3.1. In both methods, the uncertainties are dominated by the variation of the line width with wavelength. The second method overestimates the pixel size in the longer wavelength sub-bands, where the spectral bins are smaller. Table 6.2 also shows the approximate sizes (in detector pixels) of the overlapping regions between the corresponding sub-band and the following sub-band.

A crucial aspect of the MRS performance has to do with the sampling of unresolved spectral features. Zemax models predicted an undersampling of the unresolved etalon lines for channel 1, below the Nyquist frequency. More specifically, modelling has shown that the FWHM of an unresolved spectral line, as provided by the optical system, is sampled by less than the two required detector pixels. In the modelling, this applies to most sub-spectra. For channels 1, 2 and 3 spectral lines are predicted to have a FWHM of about 0.9 pixels for point sources, and 1.4 pixels for extended sources. Table 6.2 indicates that the lines are well sampled with at least the 2 pixels, with the exception of sub-band 1A, where the resolution element is slightly smaller than 2 pixels.

Overlapping regions of 100 pixels or larger are desirable for an optical matching of the different sub-bands during the science extraction of the spectra. Table 6.2 shows that this is the case for most of the overlapping regions, with some exceptions (sub-bands 1C, 3B, 3C), where the overlapping region is smaller. Nevertheless, the full wavelength range from 4.9 μm to 28.4 μm is fully covered and well sampled.

Sub-band	λ_{min} [μm]	λ_{max} [μm]	R	$\Delta\lambda_1$ [px]	$\Delta\lambda_2$ [px]	Overlap [px]
1A	4.91	5.79	3200	1.9(0.2)	1.9(0.2)	180
1B	5.60	6.62	3200	2.0(0.2)	2.0(0.2)	150
1C	6.46	7.63	3100	2.0(0.2)	2.0(0.2)	80
2A	7.55	8.91	2800	2.2(0.2)	2.2(0.2)	140
2B	8.71	10.34	2700	2.2(0.2)	2.2(0.1)	275
2C	9.89	11.71	2750	2.2(0.2)	2.3(0.2)	105
3A	11.50	13.59	2500	2.4(0.2)	2.5(0.2)	170
3B	13.19	15.58	2000	3.1(0.3)	3.4(0.4)	65
3C	15.40	18.14	2200	3.0(0.3)	3.0(0.3)	70
4A	17.88	21.34	1500	3.3(0.3)	3.7(0.3)	170
4B	20.69	24.68	1600	3.6(0.3)	4.3(0.1)	165
4C	23.83	28.43	1400	4.1(0.1)	7.2(1.1)	-

Table 6.2 The spectral properties of the MRS sub-bands. Uncertainties are indicated in parenthesis.

Fig. 6.15 shows the measured resolving power for the full wavelength range. The calibrated wavelengths are shown on the *x* axis, and the resolving power on the *y* axis. We plot these values for all the positions within the FOV. The thick black areas are the pile-up of individual black solid lines corresponding to $R(\lambda)$ calculated at different spatial (α,β) coordinates in the FOV. They give an indication of the variations of the resolving power with position on the IFU. The solid red lines are the spatially averaged values of *R*.

The instrumental requirement for resolving power states that MIRI shall provide integral field spectroscopy with spectral resolving power $R > 2400$ between 5 μm and 10 μm $R > 1600$ from 10 μm through 15 μm and $R > 800$ from 15 μm through 27 μm. Our results indicate that we are well above these requirements.

6.4.2 Variations of R with wavelength and position in the field

In general, for a particular sub-band the resolving power increases with wavelength. There is a dispersion in the measured value of *R* from the widths of individual unresolved lines of the order of 10%. Noise in the data and the effect of fringing can be responsible for this dispersion. Nevertheless, we can estimate the resolving power for an extended source with 10% uncertainty. Although lines at channel 4 are detected with less S/N, they are sampled by more pixels in the detector, and hence the dispersion in the line-to-line width does not increase dramatically.

We now investigate the variation in the resolving power with the position of the point source in the field. More specifically, we want to study how *R* changes as we move the point source across a spatial slice in the cube, and also from slice to slice. For this we use

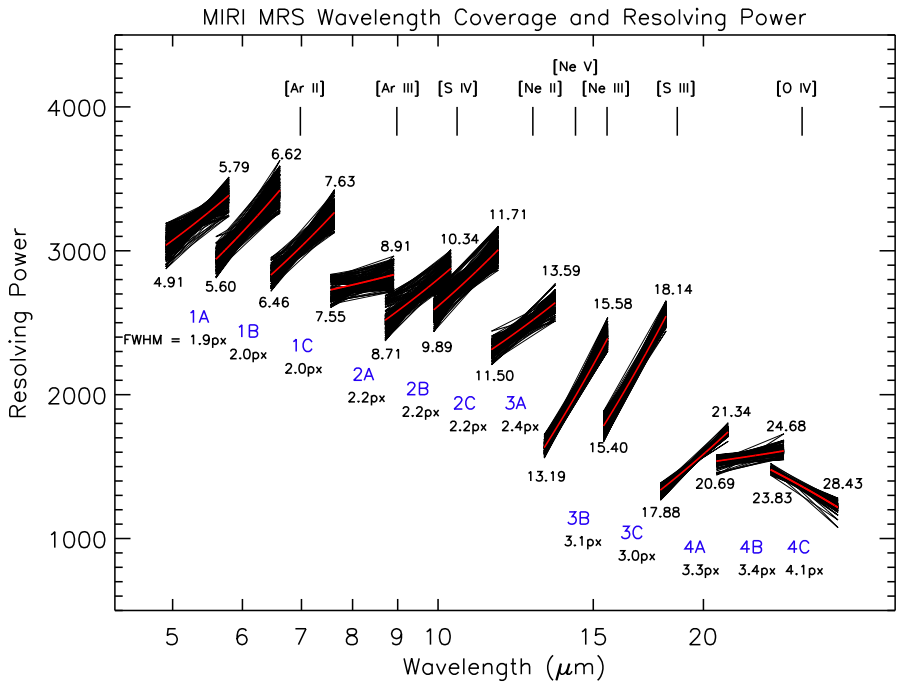

Figure 6.15 The Resolving Power of the MRS. The wavelength ranges for each sub-band are indicated. Red lines correspond to the spatially averaged values of *R*. Some relevant mid-IR nebular lines are indicated.

the point source observations that we have described in §6.2.2. In Fig. 6.16 we show the reconstructed image of the point source for one of the positions shown in Fig. 6.2, for two of the sub-bands: 1A and 4A. Unfortunately, the PSF of the 100 μm pinhole point source has some structure and does not allow for a detailed study of the PSF size as a function of wavelength. However, our purpose here is not the characterisation of the PSF, but the study of spatial variations of *R*.

Using the same method as with the extended source, we have measured the spectral resolving power as a function of position of the source. Fig. 6.17 shows the linear fit to the line widths for the three grating positions of channel 1, as the point source moves across the slice for the two different field positions shown in Fig. 6.2. Variations in resolving power when the point source moves across the slice are of the order of 1% and are within the error bars of the individual line widths. On the other hand, variations associated with placing the point source in different slices are of the order of 5% as seen in the Fig. 6.17. In sub-band 1A, the resolving power difference is larger for shorter wavelengths, while for the other sub-bands, the differences remains about the same for the sub-band range. Although close-by in the MRS FOV, the two fields are far apart in the detector space,

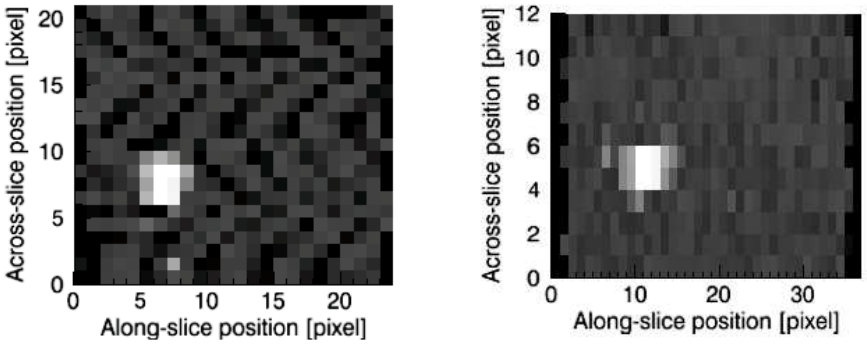

(a) Sub-band 1A (b) Sub-band 4A

Figure 6.16 The reconstructed point source at a specific wavelength for sub-bands 1A *(a)* and 4A *(b)*, for a particular position of the raster scan.

and hence the variations seen in Fig. 6.17 should give us a good estimate of the spectral resolution variations across the full FOV.

6.4.3 Line shape and spectral ghosts

We used the extended source observations to look for spectral ghosts in the spectra and to study the profile shape of the measured etalon lines. To accurately measure the average line shapes across the wavelength range of each sub-band, we shifted all lines in a given sub-spectrum using the Gaussian parameters, so that they all share the same centroid and baseline, in a similar way as we did in §5.4.4 with VM data. We have previously dubbed this method "superresolution". For the FM data, the wavelength range used to perform the superresolution extraction equals about twice the separation between etalon lines, centered on the common line centroid for each sub-band.

Fig. 6.18 shows the superresolution data for all sub-bands. We do not detect any unexpected spectral features along the spectra, apart from the almost perfectly Gaussian profile of the etalon lines. We have performed the same procedure for several random positions in the FOV with similar results. Any spectral ghost arising in the gratings is below the rms noise of the resulting superresolution etalon line, which varies between 0.5% and 1.5% of the line peak. The plots of Fig. 6.18 also show that the line shape is very symmetric for all sub-bands, only deviating slightly from a perfect Gaussian in the wings, specially for the longer wavelength sub-bands.

6.4.4 Wavelength stability

We investigated the temporal wavelength stability of the MRS by looking for variations in time of either the etalon line centroids, or the Fabry-Perot fringing pattern over periods

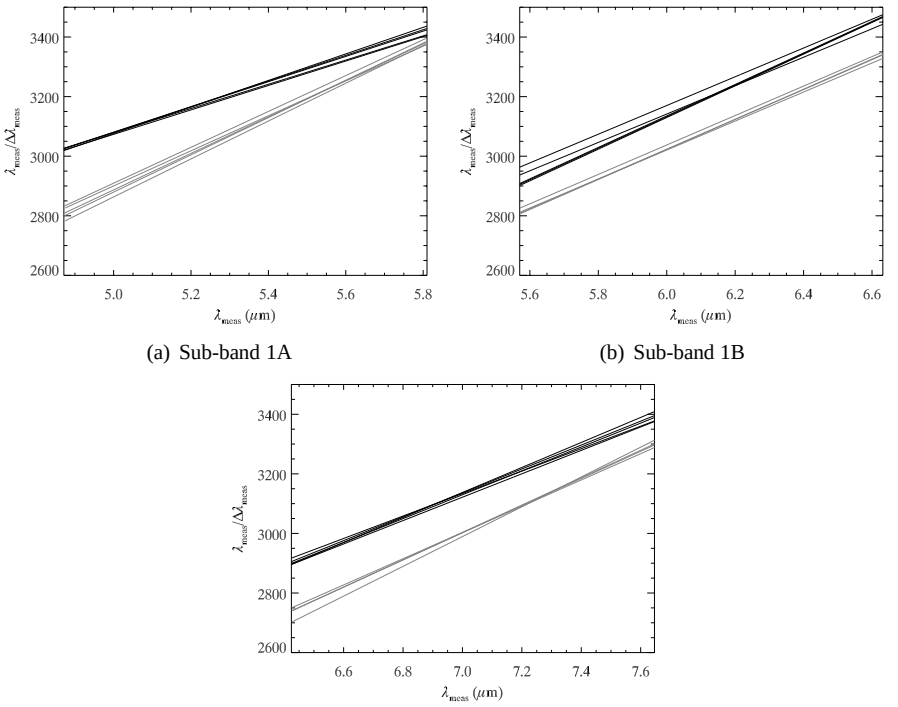

(a) Sub-band 1A

(b) Sub-band 1B

(c) Sub-band 1C

Figure 6.17 The variations in resolving power in sub-bands 1A (a), 1B (b) and 1C (c). Lines of the same color indicate the same field, or position in the FOV, as indicated in Fig. 6.2. Field 1 is in black, while Field 2 is in grey.

of time of several weeks. The science goals of MIRI require a temporal wavelength stability better than 2% of the size of the resolution element. To verify if we are within the requirements, we used the extended source etalon exposures that we have obtained at different epochs of the test campaign, as described in §6.2.2, as well as fully illuminated BB exposures, with the fringe pattern.

Time variations in wavelength

Fig. 6.19 shows the difference in sub-band 1B etalon line positions for the different epochs, with respect to the reference epoch, May 19. The result indicates that the overall shift in the etalon line positions from epoch to epoch is larger than the overall line-to-line spread. The differences are in general larger than the instrument requirement, 2% of the resolution element. In fact, for June 21 and July 10 the shift with respect to the reference positions reach about ~ 8% of the resolution element size. Some additional facts help our interpretation of this result.

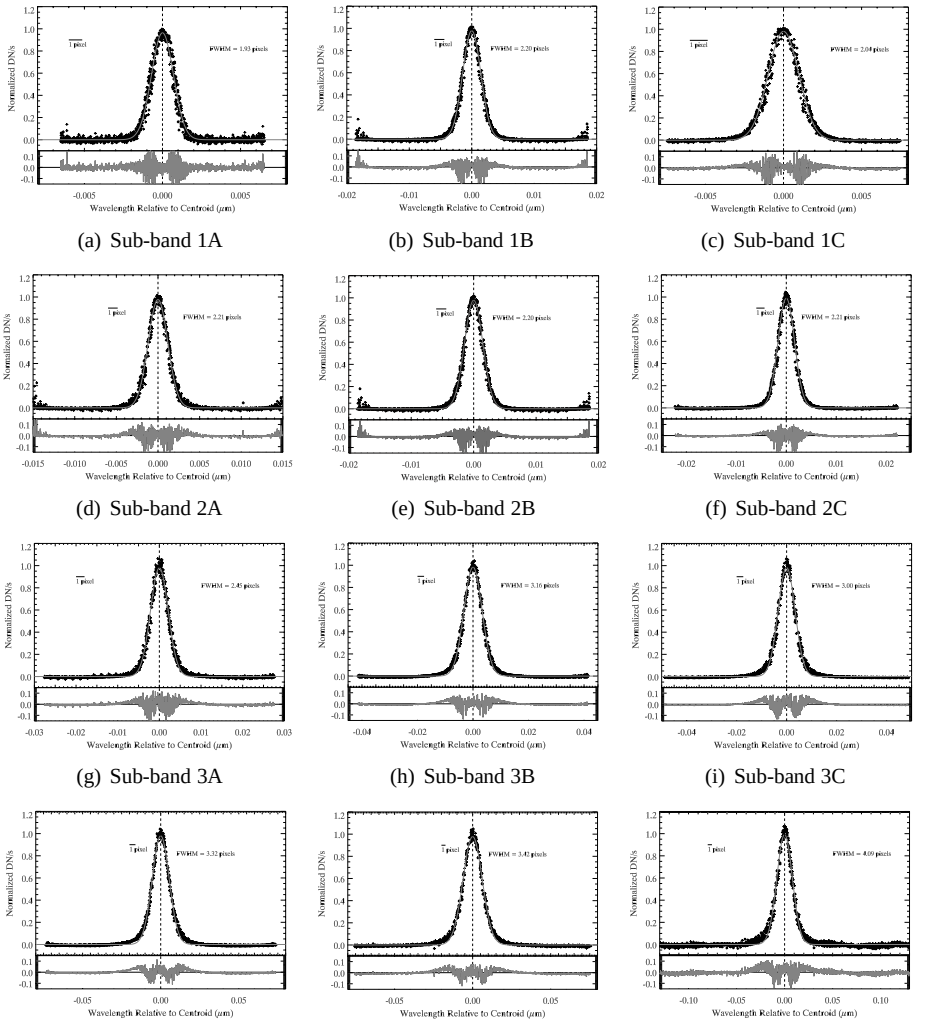

(a) Sub-band 1A (b) Sub-band 1B (c) Sub-band 1C

(d) Sub-band 2A (e) Sub-band 2B (f) Sub-band 2C

(g) Sub-band 3A (h) Sub-band 3B (i) Sub-band 3C

(j) Sub-band 4A (k) Sub-band 4B (l) Sub-band 4C

Figure 6.18 Spectral line shapes. The etalon lines in a particular field position shifted to have a common centroid. The grey line is a Gaussian fit to the resulting data. Residuals of the Gaussian fit are shown in the individual lower panels and the pixel size and FWHM of the line are indicated.

Two thermal cycles of the instrument took place between the observation epochs, on May 19 and June 21. We can not rule out that the observed shifts are the result of changes in the external conditions between these thermal cycles, rather than limitations on the stability of the spectrometer optics. Between June 21 and July 10 there were no power

or thermal cycles of the instrument and at least one of the two exposures taken on June 21 shows differences in line positions that are within the required 2% of the resolution element. According to our results, the most dramatic shift in position within a single thermal cycle is related to the reconfiguration of the grating wheel mechanism. This shift is of about 5% of the resolution element as illustrated by the light grey and dark grey diamonds in Fig. 6.19.

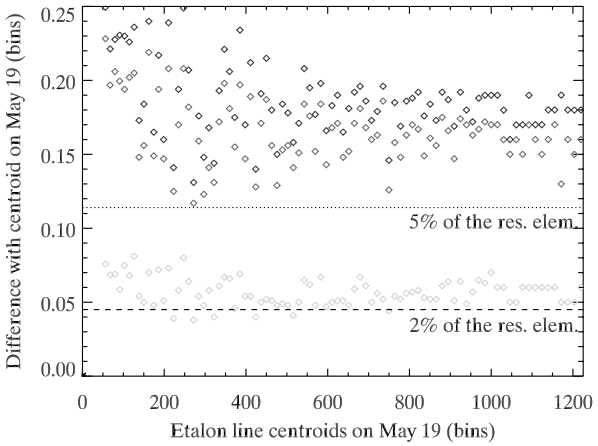

Figure 6.19 Shifts in the measured sub-band 1B line centroids with respect to the centroids on the reference epoch, May 19, in units of cube bins. Dark grey diamonds are for June 21, light gray diamonds for the same date after reconfiguring the grating mechanism and black diamonds are for July 10. The dashed line corresponds to a difference with the reference epoch of 2% of the resolution element, while the dotted line corresponds to 5% of the resolution element.

Variations with field position

Fig. 6.20 shows the variation of the shift in centroid positions for sub-band 1B, as a function of time and field position. The data points correspond to the mean value of the shift across the entire wavelength range of sub-band 1B, for three different field positions, corresponding approximately to the center of the FOV and two diagonal corners. The temporal variations in the position of the centroids is practically the same for all three field positions. This suggests that the shift is uniform across the entire field of view. The change in position for the lines measured after reconfiguration of the grating wheel on June 21 is of about 5% of the resolution element.

In particular, the shift in the etalon positions after the grating wheel mechanism is reconfigured is approximately the same across the field of view. During the period of time between the two exposures on June 21, temperature variations of the etalons did not

exceed 0.1 K, according to telemetry data. This is far too small to cause any noticeable changes in the peak positions. As a reference, our thermal models of the etalons indicate the a change of temperature in 1 K would only produce a chance of 0.9% of the resolution element in the line positions.

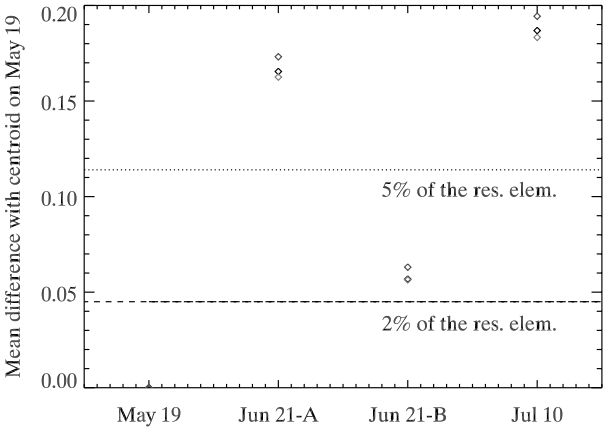

Figure 6.20 Mean shift in the line centroid positions as a function of epoch and field position. Data points correspond to the center of the FOV (black diamonds), the bottom left corner (light grey diamonds) and upper right corner (dark grey diamonds).

Variations with grating wheel configuration

If the shift in line centroids is due to mechanical reproducibility in the grating wheel, we expect a random behavior in the line shifts from sub-band to sub-band, rather than a similar behavior for all sub-bands. The reason is that the latter situation would indicate a variation on the conditions from epoch to epoch, rather than the random mechanical variations in position of the gratings after several reconfigurations.

We have used data taken for all three grating wheel positions in channel 1 to study the sub-band to sub-band variations. Additionally, we have measured the positions of the lines for the four epochs in sub-band 2A. For channel 3B, we have data available on May 19 and July 12. Fig. 6.21 shows the mean variations with respect to May 19 for the sub-bands for which we have data. The mean centroid positions were measured at a particular location in the field of view, namely the FOV center. There is no evidence of a uniform or monotone increase in the position differences with epoch. Instead, the behavior appears random from sub-band to sub-band, which favors mechanical reproducibility as the reason for the shifts.

We should expect shifts in the position of the spectra associated with hardware differences between the optics of the various gratings. However, we would not expect to

measure a shift between two spectra obtained with the same grating, after a reconfiguration has been performed. Unless, of course, these shifts are due to mechanical reproducibility. Our measurements made on June 21 indicate that, for all measured sub-bands, reconfiguration of the wheel introduced noticeable shifts, the smallest one being for sub-band 2A, close to 2% of the resolution element. Once again, this points to mechanical reproducibility as the source of the shifts.

The relative grating-to-grating tolerances of the as-designed grating hardware when all degrees of freedom are considered (translation along the z axis and rotation about all three spatial axes) have error budgets that translate into shifts in position of spectral features of about 2.5 detector pixels. As we have mentioned, these errors are repeatable to accuracies beyond what we can measure and therefore, it is likely that differences between the positions of the lines after the grating wheel mechanism has been reconfigured are due to errors in the wheel mechanism itself.

Fringe stability

So far we have studied stability relying only on the etalon lines. However, we can not rule out that the shifts that we have measured are related to stability issues in the filters or conditions of the telescope simulator itself, rather than the MRS opto-mechanics. The Fabry-Perot fringe pattern formed due to multiple reflections within the detector substrate is independent of the MTS, and thus an ultimate diagnostic for wavelength stability. We have performed an analysis of the fringe stability to confirm if the shifts measured in the etalon line centroids are due to MIRI mechanical repeatability issues, or if they arise already in the MTS.

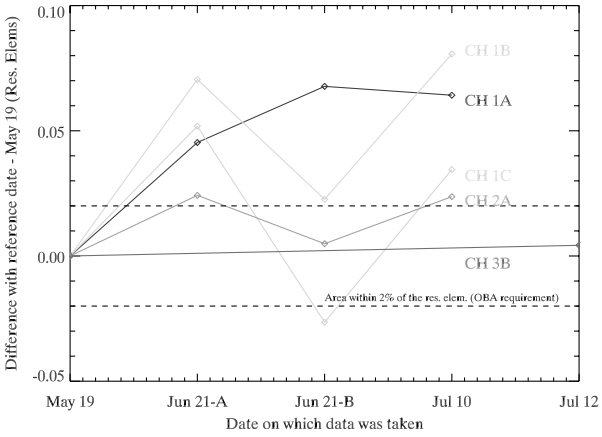

Figure 6.21 Mean shift in the line centroid positions as a function of epoch and grating wheel configuration. Data points correspond to the center of the FOV. The 2% of the resolution element requirement is shown as the two dashed lines.

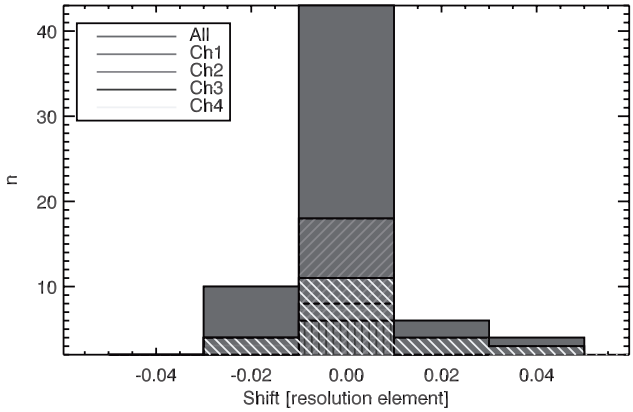

Figure 6.22 Distribution of relative shifts of the fitted fringe pattern at different epochs for all MRS channels.

We have studied the stability of the MRS over multiple epochs using fully illuminated blackbody observations. The analysis was done for a region of a particular detector slice (or a small area of the FOV), for all channels. We extract the fringe spectra at several epochs, and fit a model spectrum to each of them. We then determine relative spectral shifts from these fits using the IDL routine `CORREL_OPTIMIZE`, which finds the effective shifts (in pixels) between two arrays. Fig. 6.22 shows a distribution of the observed shifts in resolution elements (assuming a FWHM of 1.9, 2.2, 3 and 3.7 pixels for the respective MRS channels, from Table 6.2). The data show that the pixel shifts are in general less that 0.02 resolution elements), which implies compliance with the instrument requirement.

These results implies that the shifts observed in the etalon line centroids over different epochs, which are of the order of 5% of the resolution element, arise in the etalons themselves, and not in the MRS. If the shift was produced inside MIRI, then we would have observed a similar shift in the fringe pattern.

6.5 Summary

We have performed the wavelength calibration of the Flight Model Integral Field Spectrograph of the MIRI instrument, which will fly onboard the *James Webb Space Telescope* in 2018. We have described the data cube reconstruction from raw data, and used the synthetic unresolved etalon lines and wave-pass filters to calibrate the wavelength ranges and resolving powers for all 4 instrument channels. We have shown that the instrument complies with the instrumental requirements in resolving power and wavelength stability that are set by the MIRI science goals. Here is a summary of our main findings.

1. After ground data processing and application of the calibration data, we have measured the wavelengths of the MRS spectra within 2% of the size of the resolution

element, using unresolved etalon lines that are measured with signal to noise ratios well above 100.

2. The shortest wavelength registered by the MRS is 4.91 μm and the maximum registered wavelength is 28.43 μm. Within a tolerance of about 3 resolution elements, we are thus compliant of the instrumental requirement regarding wavelength coverage. Absolute calibration of sub-band 4C was made based on the Zemax model of the instrument.

3. Band overlaps between sub-bands span a range of at least 70 pixels. This allows for a smooth matching of the different sub-spectra to produce a final science result with continuous coverage of the full wavelength range.

4. The resolving power of the MRS between 5 and 10 μm is greater than 2400. From 15 μm to 28 μm, the resolving power is always larger than 1200. If we account for the intrinsic shapes of the etalon lines, we see an increase in the resolving power of between 10% and 20% with respect to these values.

5. The spectral resolution element of the MRS is sampled by at least two detector pixels for the full range of the spectrometer, except for sub-band 1C, where the resolution element is 1.9 pixels wide.

6. Variations of the resolving power across an individual FOV slice are are below the level of uncertainty introduced by the error in the statistical width of the etalon lines (about 1%), while changes of 5% in R are produced by moving the point source from slice to slice.

7. The MRS wavelengths are stable to a level below 2% the size of the resolution elements, both over long periods of time ($\sim$ 1 week) and after reconfiguring the grating wheel mechanism.